

Multiple-scattering-induced "ghost echoes" in GPM DPR observations of a tornadic supercell

Original

Multiple-scattering-induced "ghost echoes" in GPM DPR observations of a tornadic supercell / Battaglia, A.; Mroz, K.; Tanelli, S.; Tridon, F.; Kirstetter, P. -E.. - In: JOURNAL OF APPLIED METEOROLOGY AND CLIMATOLOGY. - ISSN 1558-8424. - 55:8(2016), pp. 1653-1666. [10.1175/JAMC-D-15-0136.1]

Availability:

This version is available at: 11583/2807814 since: 2020-03-31T18:52:18Z

Publisher:

American Meteorological Society

Published

DOI:10.1175/JAMC-D-15-0136.1

Terms of use:

This article is made available under terms and conditions as specified in the corresponding bibliographic description in the repository

Publisher copyright

(Article begins on next page)

Multiple-Scattering-Induced “Ghost Echoes” in GPM DPR Observations of a Tornadoic Supercell

ALESSANDRO BATTAGLIA

National Center for Earth Observation, and Earth Observation Science, Department of Physics and Astronomy, University of Leicester, Leicester, United Kingdom

KAMIL MROZ

National Center for Earth Observation, University of Leicester, Leicester, United Kingdom

SIMONE TANELLI

Jet Propulsion Laboratory, California Institute of Technology, Pasadena, California

FREDERIC TRIDON

Earth Observation Science, Department of Physics and Astronomy, University of Leicester, Leicester, United Kingdom

PIERRE-EMMANUEL KIRSTETTER

Advanced Radar Research Center, National Weather Center, and NOAA/National Severe Storms Laboratory, Norman, Oklahoma

(Manuscript received 19 May 2015, in final form 14 April 2016)

ABSTRACT

Evidence of multiple-scattering-induced pulse stretching for the signal of both frequencies of the Dual-Frequency Precipitation Radar (DPR) on the Global Precipitation Measurement (GPM) mission *Core Observatory* satellite is presented on the basis of collocated ground-based WSR-88D S-band observations of an extreme case: a tornadoic supercell. The ground-based observations clearly show a tilted convective core with a so-called bounded weak-echo region—that is, locations where precipitation is absent or extremely light at the ground while large amounts of liquid or frozen precipitation are present aloft. The satellite observations in this region show reflectivity profiles that extend all the way to the surface despite the absence of near-surface precipitation: these are here referred to as “ghost echoes.” Furthermore, the Ku- and Ka-band profiles exhibit similar slopes, which is a typical sign that the observed power is almost entirely due to multiple scattering. A novel microphysical retrieval that is based on triple-frequency (S–Ku–Ka) observations shows that a dense ice core located between 4 and 14 km with particle sizes exceeding 2.5 cm and integrated ice contents exceeding 7.0 kg m^{-2} is the source of the ghost echoes of the signal in the lower layers. The level of confidence of this assessment is strengthened by the availability of the S-band data, which provide the necessary additional constraints to the radar retrieval that is based on DPR data. This study shows not only that multiple-scattering contributions may become predominant at Ka already very high up in the atmosphere but also that they play a key role at Ku band within the layers close to the surface. As a result, extreme caution must be paid even in the interpretation of Ku-based retrievals (e.g., the TRMM PR dataset or any DPR retrievals that are based on the assumption that Ku band is not affected by multiple scattering) when examining extreme surface rain rates that occur in the presence of deep dense ice layers.

 Denotes Open Access content.



This article is licensed under a Creative Commons Attribution 4.0 license.

Corresponding author address: Alessandro Battaglia, University of Leicester, University Road, Leicester LE1 7RH, United Kingdom.
E-mail: ab474@le.ac.uk

DOI: 10.1175/JAMC-D-15-0136.1

1. Introduction

Spaceborne active systems are the backbone of the Global Earth Observation System for profiling atmospheric aerosols, clouds, and precipitation. The interpretation of the received powers from such systems is made more complicated by their large footprints, which can result in a greater fraction of the backscattered radiation having undergone multiple scattering (MS). While MS studies did historically start within the lidar community, in more recent years they have thrived within the spaceborne atmospheric radar community as well [see Battaglia et al. (2010) for a comprehensive review]. The launch in 2014 of the *Core Observatory* of the Global Precipitation Measurement [GPM; details in Hou et al. (2014)] mission with its Dual-Frequency Precipitation Radar (DPR) operating at the Ku (13.6 GHz) and Ka (35.5 GHz) bands has shed new light on this phenomenon, which has been already extensively documented for *CloudSat* W-band radar observations (e.g., Battaglia and Simmer 2008; Battaglia et al. 2008).

For radars operating in the Ku and Ka bands, MS is generally associated with ice-laden convective towers in thunderstorms. As a result, not only does MS have the potential to hamper studies of severe thunderstorms at the global scale with GPM, but, in hindsight, quantitative precipitation estimates of heavy-precipitation events retrieved from observations made with the Ku band of the Tropical Rainfall Measuring Mission Precipitation Radar (TRMM PR) should be revisited as well. Battaglia et al. (2015) highlighted the first observational evidence of MS effects in DPR observations. In that paper, the anomalous behavior of the dual-wavelength ratio [DWR; viz., the difference between the observed Ku-band and Ka-band radar reflectivity factors when expressed in reflectivity decibels (dBZ)] and the appearance of a knee-shaped DWR profile in a deep-convective case study over Sudan are discussed. The DPR footprints (5 km at nadir) are large enough to make DPR prone to MS, particularly when observing deep-convective thunderstorms, as anticipated by theoretical predictions that were based on numerical simulations (Marzano et al. 2003; Battaglia et al. 2006, 2014). In that study, however, no ground validation was available: MS effects were proposed only as a very plausible explanation to achieve consistency between the two DPR frequency observations. Furthermore, in the absence of nonattenuating-frequency radar data, only the impact of MS on the Ka-band channel could be demonstrated beyond reasonable doubt. Although the forward models suggested presence of MS also in the Ku-band data, such determination could not be made at the same level of confidence as for Ka with the available observations.

The modeling results clearly indicate that MS can also affect the Ku-band data. Thus, it is essential that this specific aspect is validated more carefully for two reasons: 1) to provide guidance to ongoing GPM DPR retrieval algorithm development the aim of which is to account for MS (some prototypes hinge upon the assumption that the Ku-band is MS free) and 2) to verify that TRMM PR was also affected by MS in hail-bearing severe storms. In fact, although several notes of caution in using TRMM data for these types of storms have been published, they do not account for this particular type of effect that, contrary to most other sources of error, can cause extremely large biases. Since its launch in February of 2014, DPR has been profiling several severe thunderstorms affected by MS: preliminary analyses that are not further discussed here indicate that essentially all profiles for which $Z_{m,Ku}$ (i.e., the observed radar reflectivity at Ku band) exceeds 45 dBZ anywhere above the zero isotherm are affected by severe MS and that profiles for which $Z_{m,Ku}$ exceeds 35 dBZ above the zero isotherm are likely to be affected by at least moderate MS (Tanelli et al. 2015).

In this paper, we focus on a tornadic supercell that was observed by the GPM DPR over Texas on 27 May 2014. This case exemplifies the occurrence of extreme MS in Ku- and Ka-band radar measurements and has the advantage of having occurred within optimal range of a ground-based weather radar. The case study serves as guidance for the interpretation of the Ku radar signal close to the ground in similar contexts (e.g., the core of the rain shaft in the same tornadic system or in any other hail-bearing severe convective storms).

Figure 1 provides an explanation of the MS mechanism for the case presented in this work. In weakly absorbing but highly scattering media, the microwave radiation transmitted by the radar is scattered several times in multiple directions. Even after several scattering events, the radiation that remained “trapped” within the receiver field of view is scattered back to the sensor and significantly contributes to the overall received signal (green lines in Fig. 1). As a result of the univocal relation between time delay and apparent range, multiply scattered radiation appears to have originated at ranges beyond distances to which it actually penetrates, with the generation of long tails [the so-called pulse stretching; see also Fig. 1 in Hogan (2008)]. In the presence of an isolated cloud/precipitation layer, this pulse stretching can produce signals well above the noise threshold in regions that are devoid of any significant target beyond the layer itself (e.g., in Fig. 1 in the blue-sky region that is located close to the surface). Hereinafter, we will refer to this effect as “ghost echoes.” Observational evidence of such an extreme phenomenon was documented for spaceborne lidar observations of liquid water clouds in which pulse stretching

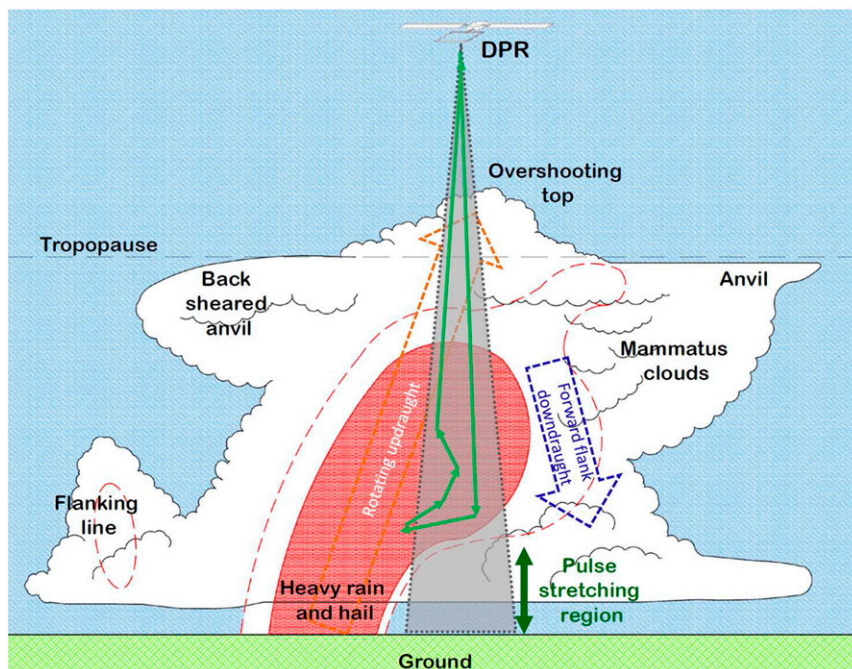


FIG. 1. Schematic for the MS pulse-stretching mechanism in a supercell that is based on the conceptual model proposed by Houze (1993) and references therein. The green lines correspond to multiply scattered radiation within the highly scattering hail-laden updraft. The red-shaded area indicates regions with reflectivities exceeding 50 dBZ at S band, and the red-dashed line corresponds to the 40-dBZ contour level. The gray-shaded region corresponds to the DPR antenna main lobe.

appeared as streaks of fading intensity below the cloud base (Miller and Stephens 1999). For the 94-GHz *CloudSat* Cloud Profiling Radar, an MS tail stretching for more than 15 km below the surface and with a signal above -16 dBZ in correspondence with a deep tropical storm cell was documented soon after launch (Im et al. 2006) and was thoroughly analyzed in Battaglia and Simmer (2008) and Battaglia et al. (2010). The first evidence of ghost echoes in the DPR dataset is discussed in this paper. In addition, this case study provides a testbed for investigating the synergistic and complementary role of spaceborne and ground-based systems. When observing severe thunderstorms, it can be used to help to define strategies for assessing potential problems, quantifying errors, and improving the GPM DPR retrieval algorithm.

The paper is organized as follows: section 2 describes the tornadic supercell event and the measurements considered in this study; section 3 discusses the key features of a specific reflectivity profile that exhibits ghost echoes in light of a microphysical retrieval that is based on the combination of ground-based and spaceborne observations; section 4 outlines some of the consequences expected for GPM DPR and TRMM PR retrievals, and conclusions are drawn in section 5.

2. The 27 May 2014 Texas event

This work focuses on a tornadic supercell that developed over southern Texas at the end of May in 2014 within a multiday severe-weather event that was associated with a slow-moving upper-level low-pressure trough. On 27 May, near-surface southeasterly warm and humid inflow from the Gulf of Mexico into a westerly dry air mass aloft led to a large and very unstable area of vertical wind shear that was favorable for the development of deep convection. A supercell thunderstorm formed south of San Antonio at 1600 local time (2100 UTC) and rapidly intensified as it moved farther to the south into more moist and unstable air, where it merged with weaker storms. The storm then developed a well-defined inflow notch and circulation. At this stage (2252 UTC), the GPM satellite captured the storm, with the overshooting top of the system located at 27.97°N latitude, 98.08°W longitude. Two tornadoes that were rated as strength 1 on the enhanced Fujita scale (EF1) formed soon after from this supercell: one caused severe damage as a result of large hail on the southeast side of Alice (27.73°N , 98.05°W) at 2315 UTC; the other affected locations in and south of Premont (27.35°N , 98.1°W). Then the storm slowly dissipated as the daytime heating ended.

TABLE 1. Time shifts between ground-based observations and the GPM overpass for different scanning angles.

Scanning angle (°)	0.57	0.97	1.41	1.89	2.55	3.21	4.08	5.18	6.50	8.04	10.06	12.52	15.64	19.53
Time shift (s)	+47	+85	−122	−107	−94	−80	−67	−54	−41	−29	−17	−4	+8	+20

a. Observations

1) GROUND-BASED OBSERVATIONS

The details of the evolution of the storm were observed by the nearby S-band (3 GHz) Corpus Christi radar (KCRP), part of the National Weather Service Weather Surveillance Radar-1988 Doppler (WSR-88D) network (Crum and Alberty 1993). During this event, the KCRP radar was operating in volume coverage pattern “212,” which is a mode designed for monitoring widespread severe convective events that used enhanced azimuthal sampling (0.5° instead of 1°) at the three lowest elevation angles so as to monitor the lower parts of precipitation systems at high spatial resolution (1.5° beamwidth and 250-m range resolution). In this configuration, the full volume scan (14 elevation angles; see Table 1) takes about 4.5 min.

At the overpass time (2252:26 UTC), the core of the precipitation system was located roughly 60 km from the KCRP radar, with no intense echo in the path between the radar and the cell of interest. These are ideal conditions to capture its 3D structure [no cone of silence, lowest elevation angles still relatively close to the surface, excellent resolution and sensitivity (down to -5 dBZ), and no attenuation issues]. Data from two consecutive volume scans were selected for comparison with the GPM overpass time. Table 1 shows the start of the KCRP WSR-88D scan start time relative to the GPM DPR measurement. Four PPIs corresponding to four different elevation angles (0.57° , 3.21° , 6.5° , and 10.06°) are shown in Fig. 2. At 60-km distance, these elevations correspond to heights of 0.6, 3.4, 6.8, and 10.6 km above sea level. The precipitation system presents several of the aspects that epitomize the characteristics of a supercell as described in Houze (1993). The lowest elevation (top-left panel) clearly shows the hook echo, which is typical of a mesocyclone circulation, with large hail producing extremely intense echoes surrounding the notch. The reflectivity patterns vary considerably with height in the storm (cf. the four panels). Of particular importance for this study is the structure of the storm at the location of the white circle, which marks the footprint of the GPM DPR profile of interest. While at low altitude that location is surrounded by an almost-clear-air region (top left), at 10.6 km (bottom right) it corresponds to the center of the reflectivity core. This setup is indicative of a tilted convective core, which is a common feature in long-lived

supercell thunderstorms. The tilted reflectivity core is a natural consequence of strong vertical wind shear that separates the updraft and downdraft within the storm. In Fig. 2, the black dots within white circles correspond to the centers of the DPR Ku- and Ka-band matched footprints; the gray continuous line is the satellite ground track.

To gain better insight into the vertical structure of the system, KCRP polarimetric data [for a full definition of polarimetric variables, refer to Bringi and Chandrasekar (2001)] have been examined along the white continuous line in Fig. 2, which coincides with the DPR cross-track sampling direction. The vertical cross section (Fig. 3) clearly shows the echo-free vault for longitudes larger than 98.08°W (top panel). Note that the behavior of all polarimetric variables (i.e., high reflectivities, low differential reflectivities Z_{DR} , and correlation coefficients ρ_{hv} that are close to 1) is consistent with the presence of hail in the slanted core. This is highlighted by the blue contour lines in Figs. 2 and 3, which correspond to the 75% probability of hail occurrence according to the detection algorithm proposed by Heinselman and Ryzhkov (2006).

2) DPR OBSERVATIONS

The DPR operates at Ku (13.6 GHz) and Ka (35.5 GHz) band, with cross-track swath widths of 245 and 120 km, respectively. Both bands have a vertical range resolution of 250 m, sampled every 125 m, and they achieve a sensitivity of better than 16 dBZ (Hou et al. 2014).

The top panels of Fig. 4 depict the vertical cross section of Ku (left) and Ka (right) reflectivity along the GPM cross track shown as a white line in Fig. 2. The storm is moving toward the east-southeast, roughly in the same direction as the cross-track scanning of the DPR. The Ku reflectivity (top-left panel) very nicely captures the tilted convective core, the overshooting top, the anvil, and the back-sheared anvil. These are all characteristic features of tornadic supercells as reproduced in the cartoon of Fig. 1.

The same features appear also in the Ka channel, although attenuation is driving the signal to the noise level for large areas close to the surface. The dual-wavelength ratio (bottom-left panel) presents the characteristic knee peaking at heights between 4 and 10 km for all profiles in the core of the system (i.e., from 97.97° to 98.2°W). As discussed in Battaglia et al. (2015), this is a

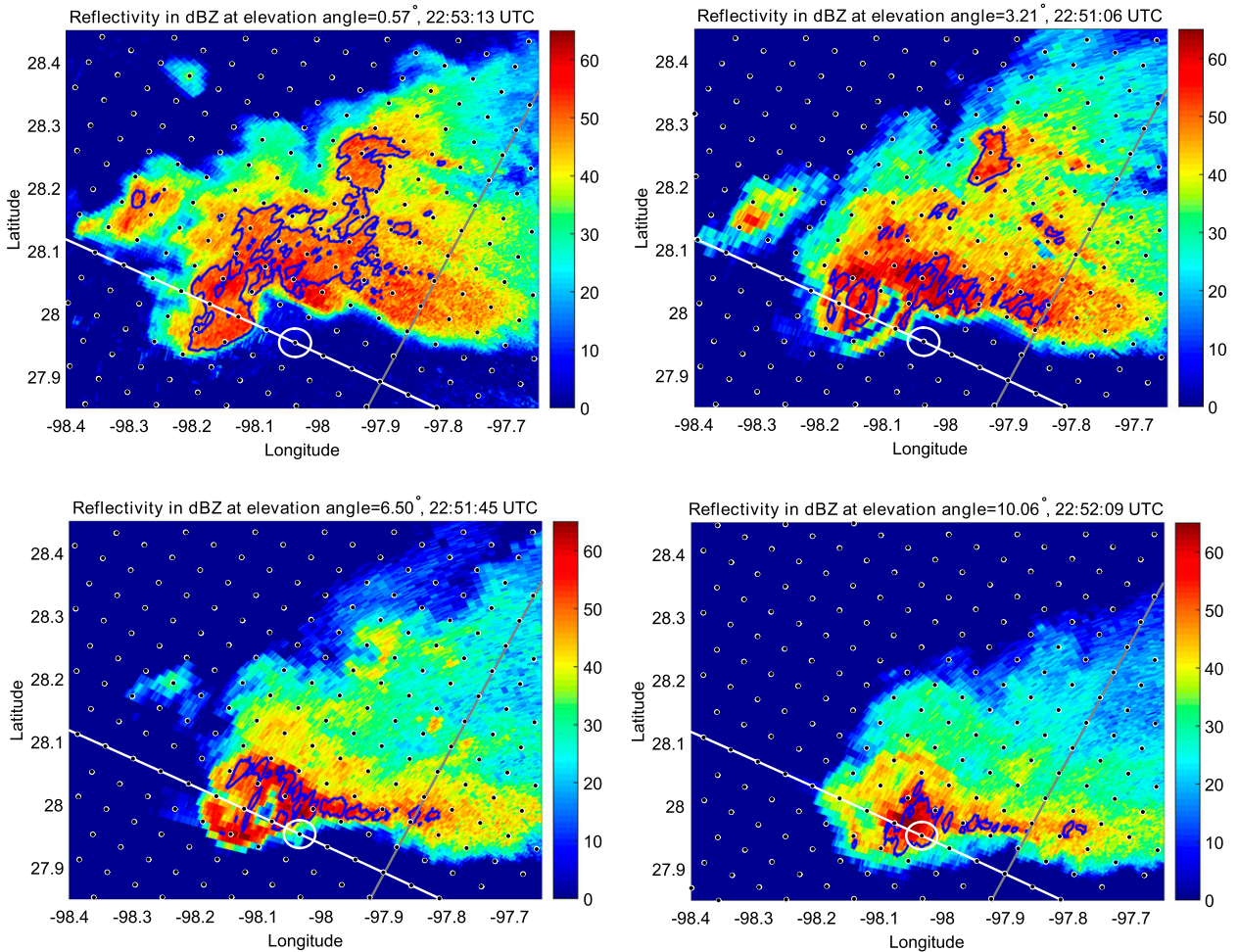


FIG. 2. Horizontal structure of the storm for four different elevation angles as captured by the KCRPS S-band radar over Texas on 27 May 2014. The white circles denote coordinates of the field of view at the corresponding height for the DPR profile that will be considered for further analysis. The blue contour lines correspond to the 75% probability of hail occurrence according to the detection algorithm proposed by [Heinselman and Ryzhkov \(2006\)](#).

clear signature of strong MS. In the following section, we describe how the high-quality S-band data were used in this case study to validate that hypothesis.

b. Synthetic S band corresponding to the DPR illumination

The WSR-88D data were used to synthesize a hypothetical S-band channel in GPM with the same beamwidth, denoted θ_{3dB} , as the DPR (i.e., 0.71°) (this would, of course, require an exceedingly large aperture of almost 10 m). Within each DPR volume of resolution (as identified by antenna pattern and pulse length), 9600 integration points were chosen by sampling 4800 different directions within the DPR beamwidth and two different points spaced by 125 m in the radial direction. The different directions are obtained in a DPR antenna-centered spherical coordinate system by sampling 120

azimuthal angles $\phi_j \in [0, 2\pi]$ and 40 polar angles relative to the antenna boresight θ_i uniformly distributed in $[0, \theta_{3dB}]$. This approach accounts for 99.91% of the reflectivity contributions within the DPR main lobe (notice that this is a span that is 2 times as wide as the nominal beamwidth). Following the method of [Ryzhkov et al. \(2013\)](#), we can neglect the effects of attenuation in the S-band signal. We have used linear interpolation of linear reflectivities to calculate the S-band reflectivity factor at each sampling point from the original KCRP volume. The synthetic GPM S-band profiles are calculated using a Gaussian approximation of the two-way antenna gain function:

$$G^2(\theta) \propto \exp[-8 \ln(2)(\theta/\theta_{3dB})^2]. \quad (1)$$

Note that for $\theta = \theta_{3dB}/2$ the gain function decreases by 6 dB, defining the nominal 5-km DPR field of view (as

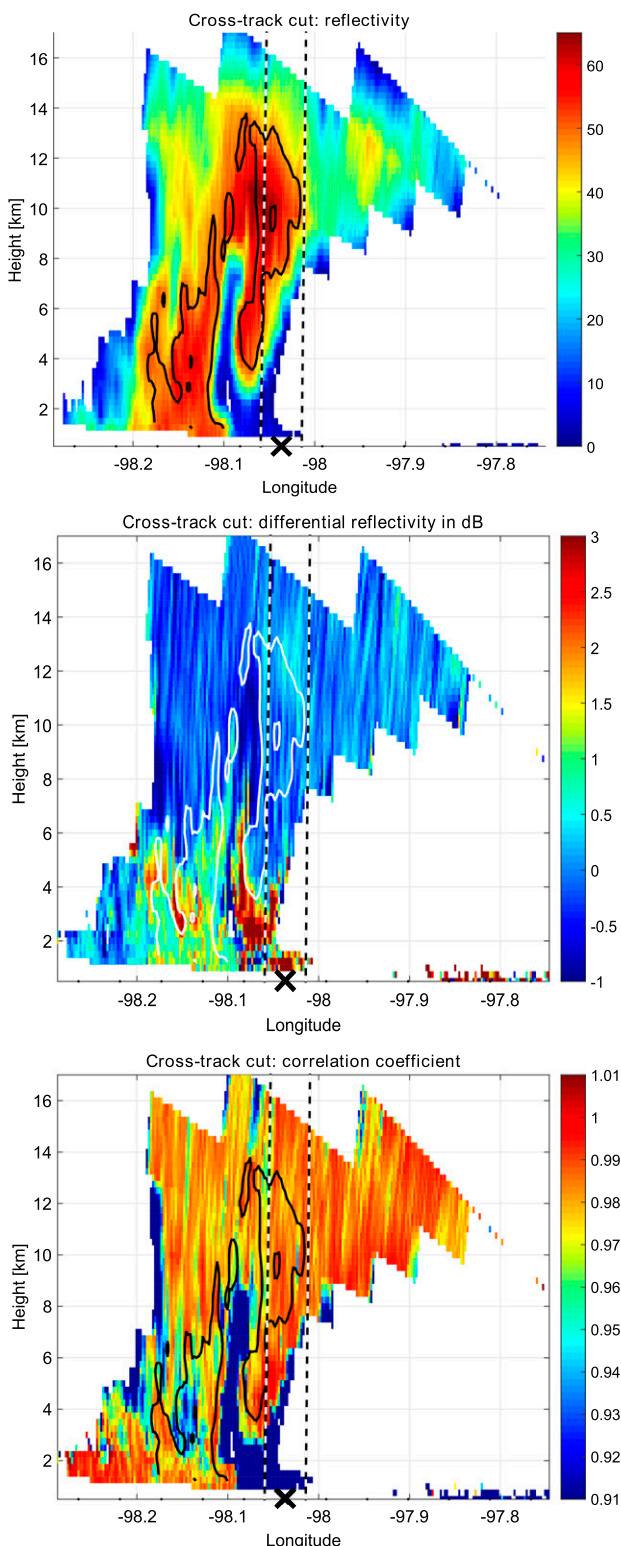


FIG. 3. Vertical structure of the storm through the white line of Fig. 2 as seen by the KCRP radar: (top) reflectivity, (middle) Z_{DR} , and (bottom) ρ_{hv} . The contour lines correspond to the 75% probability of hail occurrence according to the detection algorithm proposed by Heinselman and Ryzhkov (2006). The two dashed lines correspond to the nominal field of view of the DPR, with the projection of the boresight at the ground indicated by the black cross.

shown by the white circle in Fig. 2). The bottom-right panel in Fig. 4 represents the S-band vertical reflectivity profiles reconstructed along the DPR cross track. Despite the presence of artifacts at high altitude (due to the fact that their vertical resolution is coarser than DPR), the reconstructed S-band profiles represent a unique source of information for the following discussion by providing a “quasi Rayleigh” unattenuated reference for the measurements.

3. Detailed analysis of a bounded weak-echo region profile

The profile identified with the circle in Fig. 2 and with arrows in Fig. 4 is located in the bounded weak-echo region of the storm (see top-left panel in Fig. 2). The corresponding DPR and reconstructed S-band reflectivity profiles are depicted in Fig. 5 (red, blue, and black diamonds, respectively). Note that the local zenith angle for the DPR boresight is only 2.28° , which means that the DPR volume is almost vertical (only an ~ 400 -m shift at 10-km altitude). Because of the close proximity of the Corpus Christi radar to this profile (55.4 km), the lowest elevation observations (0.57°) allow profiling the supercell down to ~ 800 m (top-left panel in Fig. 2) at the GPM DPR boresight location.

When considering the GPM DPR vertical reflectivity profiles from the top downward, the following features are apparent.

- 1) The 18-dBZ echo-top height is located at ~ 17 -km altitude.
- 2) The Rayleigh region where Ku and Ka reflectivities are very close extends down to 16 km.
- 3) The Ka reflectivity reaches a maximum of 35 dBZ at 12 km and then, below 10 km, steadily decreases with a slope of $\sim 2 \text{ dB km}^{-1}$ all the way to the surface.
- 4) The Ku reflectivity reaches its maximum (50 dBZ) at a lower altitude (10 km) and then steadily decreases to the ground with a slope of $\sim 3.5 \text{ dB km}^{-1}$.
- 5) Both the Ka and Ku channels present clear surface peaks. Both one-way path-integrated attenuations, estimated by the surface-reference technique (0.5 and 6 dB), are strongly dominated by nonuniform beamfilling (Tanelli et al. 2012; Meneghini and Liao 2013; Meneghini et al. 2015) and will not be used in the further analysis, which is intrinsically one-dimensional. The presence of nonuniform beamfilling is clearly validated by the WSR-88D data in Fig. 6, in which the variability of S-band profiles within the DPR backscattering volume is illustrated. By looking at the percentage of profiles with signal above the 15-dBZ DPR sensitivity threshold (cyan

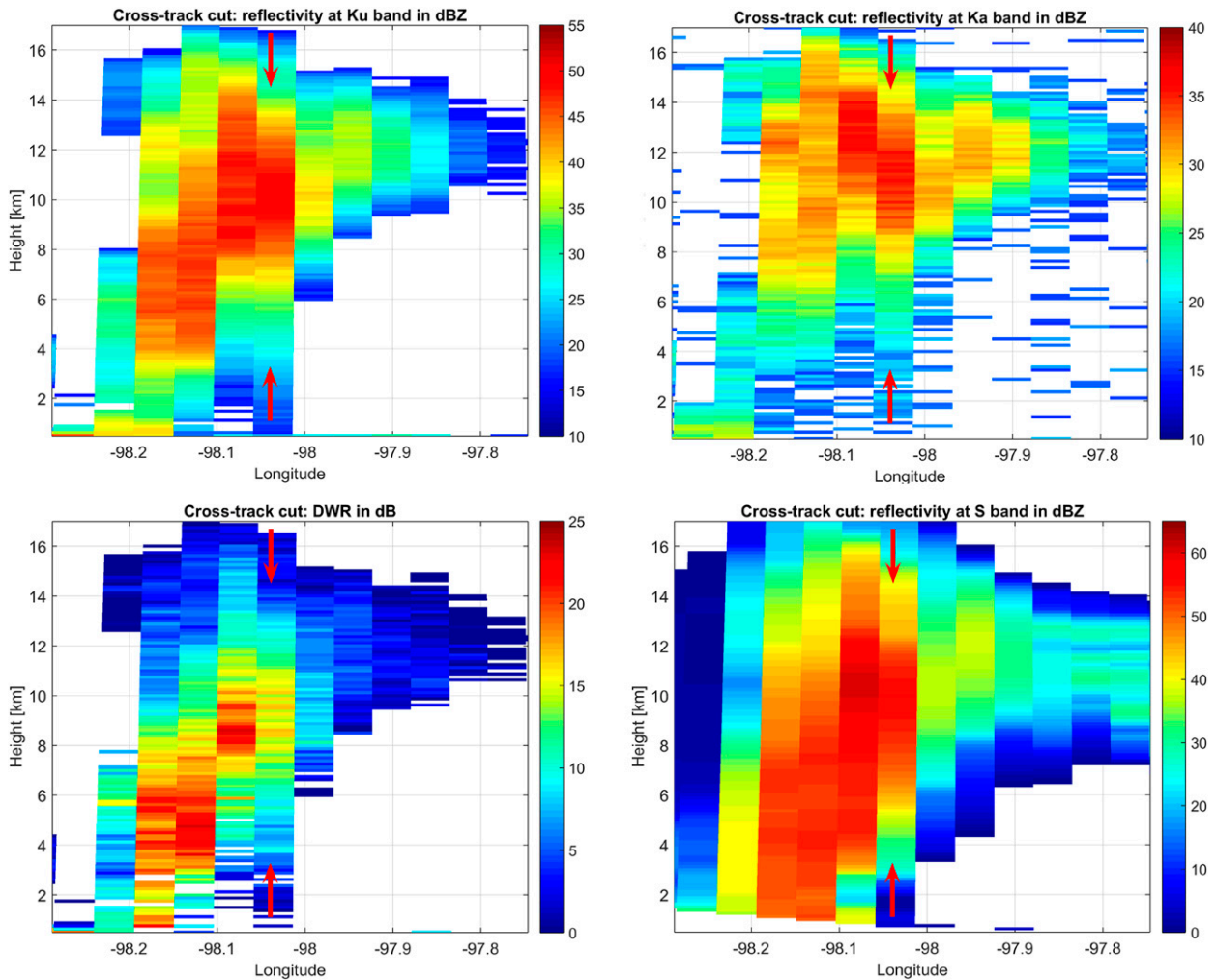


FIG. 4. Vertical cross section of (top left) Ku, (top right) Ka, (bottom left) DWR, and (bottom right) reconstructed S band for the tornadic supercell along the GPM cross track shown as a white line in Fig. 2. The arrows correspond to the profile with remarkable pulse stretching.

line), it is clear that the DPR volume is intercepting regions that are completely filled at high altitudes but that become increasingly depleted when moving from 8 km downward. The DPR volume is practically empty—meaning that its content results in backscattering that is not detectable by DPR—below 2.5 km. Of course, this contradicts the fact that both the Ku and Ka reflectivity profiles are well above the noise level practically down to the clutter-affected heights (700 m). In Fig. 6, we have also included different weighted percentiles of the original KCRP, with weights proportional to the two-way antenna gain expressed in Eq. (1). The distance between the median (50% percentile) and the mean along with the large variability between different percentiles for the KCRP reflectivities further demonstrate that

there is also a large inhomogeneity between the reflecting targets within the volume and that only a few profiles are actually contributing most of the reflectivity. For instance, at 10 km, the 5% and 95% reflectivity-weighted percentiles are between 28 and 61 dBZ.

The anomalous differential sloping (features 3 and 4 in the list above) are characteristic MS signatures, as explained in Battaglia et al. (2014, 2015). The S-band reflectivity profile reconstructed along the GPM beam supports the presence of very large ice particles in the layer between 8 and 12 km, with mean reflectivities exceeding 50 dBZ. This is also confirmed when looking at the polarimetric variables, as demonstrated in Fig. 7, in which a scatterplot in the $Z-Z_{DR}$ plane for all of the

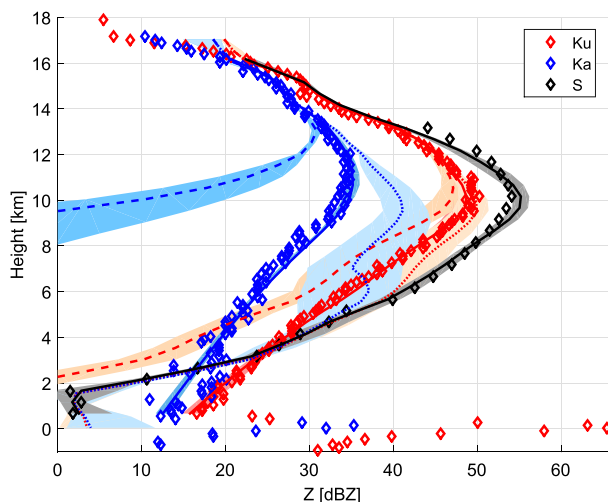


FIG. 5. Measured (diamonds) and modeled (continuous lines) reflectivities at both DPR frequencies (red and blue colors for the Ku and Ka band, respectively) and S band (black) for the profile indicated by the arrows in Fig. 4. Dashed and dotted lines correspond to the forward-modeled single-scattering and effective reflectivity profiles from the retrieved solutions, with the shadowing indicating the range of variability between the different solutions.

KCRP pixels within the DPR volume for heights between 5 and 13 km is depicted. It is clear that the majority of the points fall into the “hail” category when considering the criterion proposed by Heinselman and Ryzhkov (2006). This is particularly true for the high reflectivity values that are contributing the most to the synthetic S band reconstructed for the DPR illumination. Note also that high values of ρ_{hv} (visible in Fig. 3 at the native resolution) are typically encountered in this region, which is characteristic of hail (Ryzhkov et al. 2013).

On the other hand, the S-band profile decreases abruptly below 4 km and reaches less than 5 dBZ in the lowest 2 km. As clearly demonstrated by the vertical cross section of Fig. 4 (bottom-right panel), this is because the large hail core is slanted so that the given profile is intercepting an echo-free vault in the lower troposphere. It is remarkable that, close to the surface, the S-band reflectivity reconstructed for the GPM backscattering volume is lower than both the Ku and the Ka reflectivities, a result that is inconsistent with the expected increasingly larger amount of attenuation and Mie effects at higher frequencies. Conversely, this result is perfectly explicable if MS pulse stretching is considered, as illustrated in the cartoon of Fig. 1. The time spent by the radiation inside the ice core is the same as that required by electromagnetic waves traveling to ranges progressively closer to the surface: it appears as if targets at such ranges were backscattering radiation in a single-bounce geometry. The effect is to create a ghost

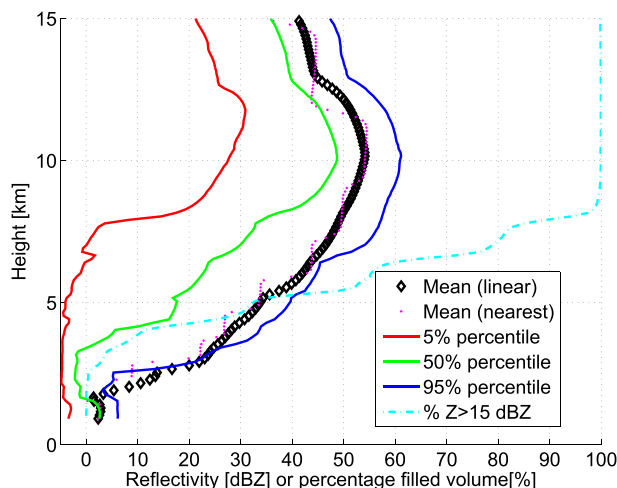


FIG. 6. Variability of S-band profiles within the DPR backscattering volume (a cylinder with a 5-km radius centered around the boresight is considered here). The mean reflectivity profile (black diamonds) is the one computed according to the procedure described in section 3. The antenna-weighted percentiles are computed for KCRP profiles. The percentage of profiles with signal above the 15-dBZ DPR-noise threshold is shown in cyan.

signal in the bounded weak-echo region at ranges for which, because of the tilted nature of this system, there are no significant atmospheric targets.

With such fast-evolving systems, the 4.5-min KCRP cycle represents a limitation with which we have to cope. As anticipated in section 1 and in Table 1, all of the KCRP low-elevation RHI scans closest to the overpass time are subsequent to the overpass time (2252:26 UTC) by a maximum delay of 85 s. Because the system is moving toward the east-southeast, we can a fortiori conclude that the bottom part of the DPR volume was indeed hitting a region that was free of significant targets in the lower troposphere. Similar pulse-stretching features were noticed in nearby profiles, but we could not rule out the presence of hydrometeors in the lowest layers as robustly as for this profile. In the future, phase-array technologies or imaging-radar techniques (Bluestein et al. 2014) will enable rapid scanning, which should be very beneficial for such comparison studies of spaceborne versus ground-based radars.

Combination of ground-based and spaceborne observations: Microphysical triple-frequency retrieval

The availability of high-quality ground-based observations offers an unprecedented opportunity for investigating the synergistic and complementary role of spaceborne and ground-based systems when observing severe thunderstorms. The ground-based system offers a “Rayleigh” image of the storm with fine details of the horizontal structure of the system but coarse vertical resolution, especially in the upper portions of the storm

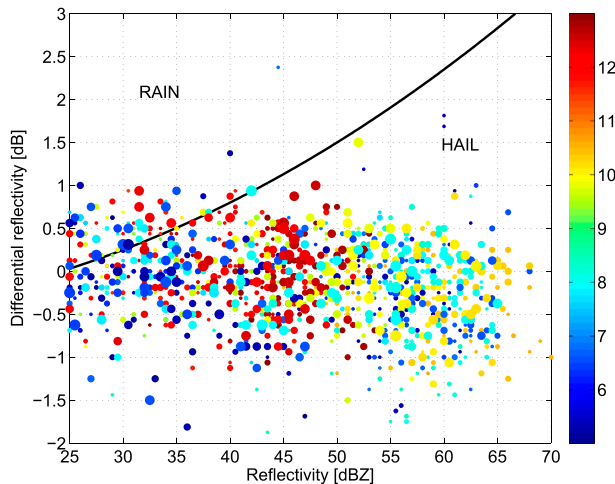


FIG. 7. Scatterplots in the Z - Z_{DR} plane for all of the KCRP pixels within the DPR volume for the profile identified by the arrows in Fig. 4 for heights between 5 and 13 km. Large and small circles are points within the satellite nominal field of view and for antenna polar angle between $\theta_{3dB}/2$ and θ_{3dB} , respectively. The color bar is modulated by the height expressed in kilometers. The black line corresponds to the boundary between rain and hail, as provided by Heinselman and Ryzhkov (2006).

(e.g., Fig. 2). On the other hand, the DPR has limited penetration capabilities in the lower levels but is capable of finely profiling the storm in the upper levels (Fig. 4). When combined together, the three-frequency data so collected considerably reduce the space of solutions and produce a seamless description of the thunderstorm structure from top (ice) to bottom (rain).

To optimally combine the suite of observations and to demonstrate the plausibility of our interpretation, a retrieval algorithm has been applied to the triple-frequency observations. The retrieval [for more details, see Battaglia et al. (2015)] is based on an optimal estimation technique (Rodgers 2000), following similar approaches proposed in the past (L'Ecuyer and Stephens 2002; Mitrescu et al. 2010). It assimilates multifrequency reflectivity profiles and additional measurements (like path-integrated attenuations). The fast code developed in Hogan and Battaglia (2008) is adopted as the forward operator for computing the reflectivity profiles and the relevant Jacobians. The code includes MS effects, but three-dimensional/nonuniform beamfilling effects cannot be properly accounted for since the code is inherently one-dimensional. This is, of course, a limitation, given the large inhomogeneity that is characteristic of this profile, as previously mentioned. A 1-dB 1-standard deviation uncertainty is adopted for the DPR reflectivities at large signal-to-noise ratio with larger values (3 dB) when approaching the minimum sensitivity values, here assumed to be 11 and 16 dBZ for the Ku and Ka DPR channels, respectively. On the other hand, the

S-band reconstructed profile is affected by spatial and temporal mismatching errors, which are particularly exacerbated at high altitudes because of the volume sampling driven by the 14 elevation angles. To partially account for that, a 2-dB 1-standard deviation uncertainty has been assumed for the S-band reconstructed profile. The assumed uncertainty also rapidly increases above 10 km. See, for example, the poor S-band sampling in Fig. 6 highlighted by the mean profile computed with the nearest-neighbor technique (magenta dots).

The algorithm retrieves profiles of equivalent water content and mean mass-weighted diameters D_m for solid and liquid hydrometeors. Different a priori (coincident with first guess) assumptions are used to initialize several alternate optimal estimation solutions:

- 1) For the ice density, values ranging from 0.1 to 0.9 g cm^{-3} are adopted, thus covering the whole spectrum of solid phase from snow to hail. Truncated exponential size distributions are used when computing the single-scattering properties of (dry) hail, as proposed in Ulbrich and Atlas (1982). The maximum hail size D_{max} has been assumed to equal to 4 times D_m .
- 2) For the height at which rain is appearing H_r , two values (i.e., 10 and 6 km) are adopted. This selection explores two bounding cases for a deep convective core: one in which liquid water reaches the highest possible altitudes and one in which it is limited to just above the zero isotherm.
- 3) For profiles of D_m , it is assumed that they peak at the height at which the liquid phase is appearing, but with several maximum sizes with a distinct range of values for each density assumption.
- 4) For the cutoff height for rain R_b , values between 0 and 4 km are assumed so as to allow for a “free hydrometeor” region in the lower atmosphere (as expected for bounded weak-echo-region profiles).

Note that melting hydrometeors (e.g., wet hail) have not been included. Some aspects of their impact on radar reflectivity profiles are here captured by the coexisting hail and rain in the same layers. This solution is certainly not capable of fully characterizing the scattering properties of such media, but it provides a simple approach for a first-order solution and avoids additional unknowns that further complicate the problem. The retrieval results within the layer in which different phases are coexisting must, of course, be taken with caution.

Of all initial-condition configurations, two categories did not result in any convergent solution: those involving low-density particles (i.e., 0.1 g cm^{-3}), and those assuming that hydrometeors were present all the way to the surface (i.e., cutoff height of 0 km). The former is

because it was unable to reproduce the MS signatures observed in DPR data, and the latter is because it was unable to reproduce the echo-free vault observed by the S-band radar. Besides these two not-surprising exclusions, the retrievals generated by those initial configurations that did converge are shown in Fig. 8. To assess the information content of the available remote sensing measurements, we first focus on the common features among them. First, we consider the ice population above the freezing level. The top panel in Fig. 8 shows that, regardless of the assumptions on ice density between 0.2 and 0.9 g cm^{-3} , all convergent solutions point at the same profile of mean mass-weighted particle size peaking at about 10-km altitude on values between 5.5 and 7 mm. As one can expect, the retrieved amount of ice water content (central panel) is inversely related to the ice-density assumption: if one assumes lower density, and therefore lower extinction and albedo per particle, the multiple-scattering signature in the profile requires increasingly larger number densities to be explained. Other than this scaling factor, all profiles agree on the vertical placement of the layer of large high-density ice: between 8 and 14 km. Even this three-frequency retrieval does not allow one to unequivocally determine the ice density and the ice contents without further assumptions, however. The last logical step in the interpretation of these candidate retrievals can only rely on general microphysical and climatological considerations that are based on the nature of this storm. For instance, it is more likely that approximately $1\text{--}2 \text{ g m}^{-3}$ of hailstone sizes up to approximately 2–2.5 cm (i.e., 4 times the mean mass-weighted diameter) and total equivalent integrated water content exceeding 7.0 kg m^{-2} were the cause of the observed radar reflectivities, rather than more than 33 kg m^{-2} with ice content peaking at 7 g m^{-3} of remarkably large rimed snowflakes (cyan lines in the top panel of Fig. 8).

Second, we look at the retrieved configuration of liquid above the zero isotherm. The bottom panel shows how the retrievals that assumed high-density hail converged almost exclusively when liquid water was also allowed to be present up to 10-km altitude. When looking at the profiles of ice water contents and rain rates (center and bottom panels), a coherent transition from uplifted raindrops to hail in the region 5 km above the freezing level appears. On the contrary, the profiles that assumed lower densities (more typical of heavy riming than raindrop freezing) converged only when confining rain to below 6 km, creating the scenario of two apparently decoupled layers of extremely large amounts of condensate separated by a depleted layer between 6 and 8 km. Although these solutions do fit the measured observables, they are very unrealistic when

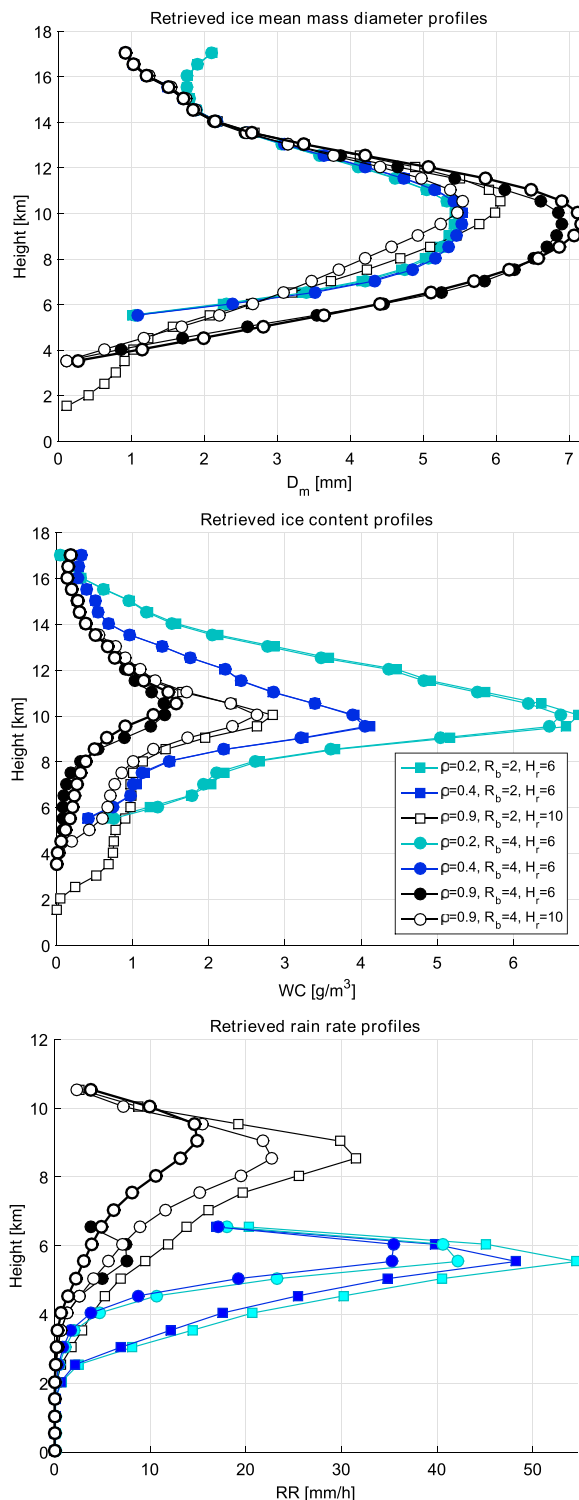


FIG. 8. Retrieved profiles of (top) ice mean mass diameters, (middle) ice water content, and (bottom) rain rates when using S, Ku, and Ka observations. Cyan, blue, and black correspond to ice densities of 0.2, 0.4, and 0.9 g cm^{-3} , respectively. The different symbols correspond to different heights at which the rain is appearing (H_r) and disappearing (R_b). Lines with different thicknesses correspond to profiles with different a priori assumptions for D_m . Note that the legend in the middle panel applies to all of the panels.

interpreted in terms of tornadic-cell microphysical processes [chapter 8 in Houze (1993)].

Third, we can focus on the lowest layer below the freezing level. Here, the information content is limited; only the S-band constraint can provide information on the amounts of hydrometeors, with the intrinsic limitations of a single-frequency retrieval. It clearly captures the absence of hydrometeors in the lowest 2 km, as one would expect, but the uncertainties above that are significant, even within the assumption of hail for the ice above. Overall, the three frequencies account for roughly 24 degrees of freedom for signal out of roughly 100 measurement points (three reflectivity profiles averaged at 500-m vertical resolution).

This three-frequency single-polarization retrieval agrees with the conclusions drawn from the polarimetric measurements (i.e., presence of hail aloft). GPM Microwave Imager observations similarly suggest brightness temperatures for the pixel corresponding to the analyzed profile that are colder than 100 K at both 89 and 166 GHz. This result is compatible only with the scenarios with 0.4 or 0.9 g cm⁻³ densities.

4. Implications for GPM DPR and TRMM PR retrieval

In Fig. 5, the single-scattering, MS (i.e., including all orders of scattering), and effective forward-modeled reflectivities (i.e., single scattering without attenuation) in correspondence with the retrieved solutions of Fig. 8 are shown with dashed, continuous, and dotted lines (with the shading indicating the residual variability of all solutions). These results suggest not only that MS contributions become predominant at Ka already very high up in the atmosphere (e.g., the single scattering is more than 7 dB below the MS signal already at 12 km) but also that they play a key role at Ku band, with the MS signal being 10 dB larger than the single-scattering signal at all heights below 4 km (cf. continuous and dashed lines in Fig. 8). This case study demonstrates that the ice-laden layer located above 6 km is generating an MS tail for the Ku radar (red diamonds in Fig. 5), sloping down at roughly 3.8 dB km⁻¹ in the lowest 6 km. In a single-scattering scenario, this same signal could be produced by a uniform high rain-rate layer generating a one-way attenuation of 1.9 dB km⁻¹. If the TRMM relationship $k_{Ku} = \alpha_{Ku} RR^{\beta_{Ku}}$ is used ($\alpha_{Ku} = 0.0225$ and $\beta_{Ku} = 1.154$, with attenuation coefficient k in decibels per kilometer and the rain rate RR in millimeters per hour; Iguchi et al. 2009), this corresponds to approximately 47 mm h⁻¹. This finding has serious implications for Ku-only retrievals in the presence of deep convection and extreme rainfall underneath. In fact, in the

presence of an ice layer like the one analyzed here, the single-scattering signal generated by high-rain-rate layers in the lower atmosphere (in this case, larger than ~50 mm h⁻¹) would be completely masked by the long tail generated by MS. In other words, the Ku band is practically blind to extreme rain rates located underneath high-density ice layers. Of course, this effect is partially mitigated if path-integrated attenuation estimates are available [although such estimates are more difficult over land and are known to be seriously affected by nonuniform beamfilling effects, particularly in deep convection; see Iguchi et al. (2009) and Short et al. (2015) for a specific example of a tilted system].

To demonstrate further where the S-band measurements add information to the DPR measurements and where they do not, the same algorithm described in section 3a, with the same set of a priori assumptions, has been run but constrained only by the DPR measurements. The results are shown in Fig. 9 and can be analyzed in comparison with Fig. 8. Ice particle size estimation is unchanged from the top to ~12-km altitude, as one could expect given the fact that for particle sizes below 4 mm the S band adds very little information with respect to the Ku-/Ka-band pair. Between 12 and 8 km, however, the only commonality among all solutions is that mean ice particle size is at least 4 mm. Beyond that point, the information content drops dramatically, and a wide range of possible solutions remain plausible in the space of observables, including many solutions in which precipitation reaches all the way to the surface (although these solutions are at odds with the surface-reference-technique-based path-integrated attenuation estimates). This reduced penetration capability is corroborated by the decreases to a value of 16 of the degrees of freedom of signal (vs 24 for the previous retrieval that included the S-band observations). In this particular profile, one can argue that the only information that DPR can provide is that of a strong indication of large hail occurring at ~10-km altitude. Per se, this is a strong piece of information when considering the global dataset of GPM: Where and when does hail occur? With respect to TRMM/PR, DPR is actually facilitated by the presence of multiple scattering at Ka- and Ku-bands in providing reliable information in this regard. This fact paves the way toward important applications that could be explored in the future, such as an extended comparison with ground-based polarimetric hail identification (e.g., via WSR-88D), thus enabling at a later stage the construction of a global climatological description of hail.

As expected, with the denial of S-band data, the solver finds different ways to explain the decrease of reflectivity in the lower atmosphere: not only by a genuine decrease

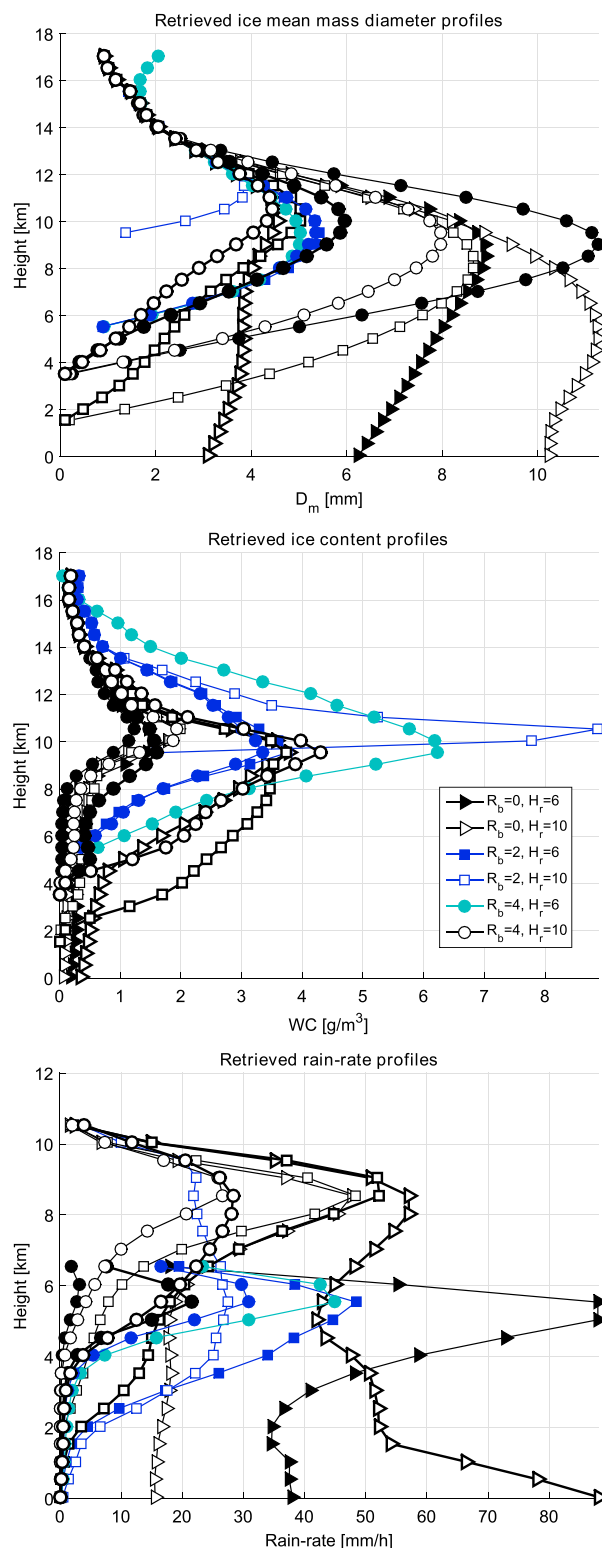


FIG. 9. As in Fig. 8, but for retrievals that use the DPR measurements only.

in the water and ice content (solutions with R_b equal to 2 or 4 km) but also by a combination of the decrease in the concentration/size of the hail particles and of the attenuation caused by rain (solutions with $R_b = 0$). One solution (the thick open triangles) shows rain rate exceeding 50 mm h^{-1} below 4-km altitude, thus fully supporting the previous reasoning. Further increasing the rain rate does not modify the measured reflectivity profile for both DPR channels. For profiles exhibiting heavy rain associated with significant scattering aloft (as expected, for instance, for the profiles located between 98.2° and 98.1°W longitude in Fig. 4) the GPM DPR and the TRMM PR observations may not be able to directly diagnose how extreme the precipitation in the bottom layer is. Because for such cases the surface precipitation variable lies in the null space (Rodgers 2000), its estimation must rely on a priori relationships with the variables that are within the observation space (e.g., the ice content aloft). Proper a priori state-variable covariance matrices can be built on the basis of statistically significant evaluation datasets, which is a topic for future research.

A final consideration: the fact that the MS tends to effectively reduce the measured reflectivity slope for extreme rain rates suggests the idea that Ku-only retrievals (e.g., those available from the TRMM dataset) could be negatively biased in such conditions, a result that seems to agree with the ground-based validation analysis conducted by Amitai et al. (2012) and Kirstetter et al. (2013). This idea prompts prudence when analyzing extreme events in the TRMM dataset. For instance, some of the conclusions drawn in Hamada et al. (2014, 2015) must be taken with caution, because MS is indeed expected to strongly bias Ku-based retrievals in deep convection but not as much in warm rain or in shallow precipitation.

5. Conclusions

Collocated GPM DPR and WSR-88D S-band observations of a tornadic supercell over Texas offer an unprecedented opportunity for understanding the potential of GPM DPR observations of extreme-weather events. Ground-based polarimetric observations show that the storm contains hail and has a tilted reflectivity structure that is indicative of a supercell thunderstorm. Both of these features are the key factors for producing MS-induced pulse stretching at both Ka and Ku band in correspondence with DPR profiles in the bounded weak-echo region, which are intercepting the hail core but not significant precipitation at the ground. As a result, inside supercells and dense ice-laden convective cells, MS effects add complexity to the interpretation of the GPM DPR signal, which is already complicated by the presence of nonuniform beamfilling effects and by a

variety of microphysical processes. In hindsight, the same applies to the interpretation of Tropical Rainfall Measuring Mission Precipitation Radar signal. As demonstrated by the extreme example described in this work, the DPR signal close to the ground can be explained by the MS tail generated by the dense ice core above. This is likely to produce additional uncertainties in surface precipitation retrievals, especially when dealing with extreme precipitation. As a rule of thumb, in the presence of deep convection, extreme caution must be paid in the interpretation of current GPM and TRMM Ku-only retrievals when dealing with retrieved rain-rate values in excess of 50 mm h^{-1} . This result has profound implications because it may alter the relative contribution of extreme precipitation to the total volume, possibly affecting also the computations of precipitation total volumes in regions/seasons in which precipitation comes mainly from system that produce dense and large ice. Along the same lines, contoured-frequency-by-altitude diagrams of effective reflectivities, which are typically used in the analyses of the life cycle of these systems, must include MS corrections in their derivation from measured reflectivity profiles. This is mandatory for obtaining genuine profiles of reflectivities and precipitation in the lower levels close to the ground.

Ongoing work is now focused on identifying the MS-contaminated profiles, on extracting all of the information content in the measurements with ad hoc retrievals, and on transferring this information into surface precipitation via climatologically based parameterizations (e.g., by adopting transfer functions that are based on S-band-based collocated datasets). The interplay between MS and nonuniform beamfilling effects is also under study.

Acknowledgments. The work done by A. Battaglia and F. Tridon was funded by the project “Calibration and validation studies over the North Atlantic and United Kingdom for the Global Precipitation Mission” funded by the United Kingdom NERC (NE/L007169/1). The work done by S. Tanelli was carried out at the Jet Propulsion Laboratory, California Institute of Technology, under a contract with the National Aeronautics and Space Administration. This work was carried out for the GPM mission under the Precipitation Measurement Missions program; support by Dr. Ramesh Kakar is gratefully acknowledged. Level-1 V03B-GPM data were downloaded from the Precipitation Processing System. KCRP data were downloaded from the National Oceanic and Atmospheric Administration National Climatic Data Center. This research used the SPECTRE High Performance Computing Facility at the University of Leicester.

REFERENCES

- Amitai, E., W. Petersen, X. Llort, and S. Vasiloff, 2012: Multiplatform comparisons of rain intensity for extreme precipitation events. *IEEE Trans. Geosci. Remote Sens.*, **50**, 675–686, doi:[10.1109/TGRS.2011.2162737](https://doi.org/10.1109/TGRS.2011.2162737).
- Battaglia, A., and C. Simmer, 2008: How does multiple scattering affect the spaceborne W-band radar measurements at ranges close to and crossing the sea-surface range? *IEEE Trans. Geosci. Remote Sens.*, **46**, 1644–1651, doi:[10.1109/TGRS.2008.916085](https://doi.org/10.1109/TGRS.2008.916085).
- , M. O. Ajewole, and C. Simmer, 2006: Evaluation of radar multiple scattering effects from a GPM perspective. Part II: Model results. *J. Appl. Meteor.*, **45**, 1648–1664, doi:[10.1175/JAM2425.1](https://doi.org/10.1175/JAM2425.1).
- , J. M. Haynes, T. L’Ecuyer, and C. Simmer, 2008: Identifying multiple-scattering affected profiles in *CloudSat* observations over the oceans. *J. Geophys. Res.*, **113**, D00A17, doi:[10.1029/2008JD009960](https://doi.org/10.1029/2008JD009960).
- , S. Tanelli, S. Kobayashi, D. Zrnicek, R. Hogan, and C. Simmer, 2010: Multiple-scattering in radar systems: A review. *J. Quant. Spectrosc. Radiat. Transfer*, **111**, 917–947, doi:[10.1016/j.jqsrt.2009.11.024](https://doi.org/10.1016/j.jqsrt.2009.11.024).
- , G. Heymsfield, and L. Tian, 2014: The dual wavelength ratio knee: A signature of multiple scattering in airborne Ku–Ka observations. *J. Appl. Meteor. Climatol.*, **53**, 1790–1808, doi:[10.1175/JAMC-D-13-0341.1](https://doi.org/10.1175/JAMC-D-13-0341.1).
- , K. Mroz, and F. Tridon, 2015: Multiple scattering in observations of the GPM Dual-Frequency Precipitation Radar: Evidence and impact on retrievals. *J. Geophys. Res. Atmos.*, **120**, 4090–4101, doi:[10.1002/2014JD022866](https://doi.org/10.1002/2014JD022866).
- Bluestein, H. B., and Coauthors, 2014: Radar in atmospheric sciences and related research: Current systems, emerging technology, and future needs. *Bull. Amer. Meteor. Soc.*, **95**, 1850–1861, doi:[10.1175/BAMS-D-13-00079.1](https://doi.org/10.1175/BAMS-D-13-00079.1).
- Bringi, V. N., and V. Chandrasekar, 2001: *Polarimetric Doppler Weather Radar: Principles and Applications*. Cambridge University Press, 266 pp.
- Crum, T., and R. Albrecht, 1993: The WSR-88D and the WSR-88D Operational Support Facility. *Bull. Amer. Meteor. Soc.*, **74**, 1669–1687, doi:[10.1175/1520-0477\(1993\)074<1669:TWATWO>2.0.CO;2](https://doi.org/10.1175/1520-0477(1993)074<1669:TWATWO>2.0.CO;2).
- Hamada, A., Y. Murayama, and Y. N. Takayabu, 2014: Regional characteristics of extreme rainfall extracted from TRMM PR measurements. *J. Climate*, **27**, 8151–8169, doi:[10.1175/JCLI-D-14-00107.1](https://doi.org/10.1175/JCLI-D-14-00107.1).
- , Y. N. Takayabu, C. Liu, and E. J. Zipser, 2015: Weak linkage between the heaviest rainfall and tallest storms. *Nat. Commun.*, **6**, 6213, doi:[10.1038/ncomms7213](https://doi.org/10.1038/ncomms7213).
- Heinselman, P. L., and A. V. Ryzhkov, 2006: Validation of polarimetric hail detection. *Wea. Forecasting*, **21**, 839–850, doi:[10.1175/WAF956.1](https://doi.org/10.1175/WAF956.1).
- Hogan, R. J., 2008: Fast lidar and radar multiple-scattering models: Part I: Small-angle scattering using the photon variance–covariance method. *J. Atmos. Sci.*, **65**, 3621–3635, doi:[10.1175/2008JAS2642.1](https://doi.org/10.1175/2008JAS2642.1).
- , and A. Battaglia, 2008: Fast lidar and radar multiple-scattering models: Part 2: Wide-angle scattering using the time-dependent two-stream approximation. *J. Atmos. Sci.*, **65**, 3636–3651, doi:[10.1175/2008JAS2643.1](https://doi.org/10.1175/2008JAS2643.1).
- Hou, A. Y., and Coauthors, 2014: The Global Precipitation Measurement mission. *Bull. Amer. Meteor. Soc.*, **95**, 701–722, doi:[10.1175/BAMS-D-13-00164.1](https://doi.org/10.1175/BAMS-D-13-00164.1).
- Houze, R. A., 1993: *Cloud Dynamics*. International Geophysics Series, Vol. 53, Academic Press, 573 pp.

- Iguchi, T., T. Kozu, J. Kwiatkowski, R. Meneghini, J. Awaka, and K. Okamoto, 2009: Uncertainties in the rain profiling algorithm for the TRMM Precipitation Radar. *J. Meteor. Soc. Japan*, **87A**, 1–30, doi:[10.2151/jmsj.87A.1](https://doi.org/10.2151/jmsj.87A.1).
- Im, E., S. Durden, S. Tanelli, and K. Pak, 2006: Early results on cloud profiling radar post-launch calibration and operations. *Proc. IEEE Int. Conf. on Geoscience and Remote Sensing Symp. 2006*, Denver, CO, Institute of Electrical and Electronics Engineers, 93–96, doi:[10.1109/IGARSS.2006.29](https://doi.org/10.1109/IGARSS.2006.29).
- Kirstetter, P.-E., Y. Hong, J. J. Gourley, M. Schwaller, W. Petersen, and J. Zhang, 2013: Comparison of TRMM 2A25 products, version 6 and version 7, with NOAA/NSSL ground radar-based National Mosaic QPE. *J. Hydrol.*, **14**, 661–669, doi:[10.1175/JHM-D-12-030.1](https://doi.org/10.1175/JHM-D-12-030.1).
- L'Ecuyer, T. S., and G. L. Stephens, 2002: An estimation-based precipitation retrieval algorithm for attenuating radars. *J. Appl. Meteor.*, **41**, 272–285, doi:[10.1175/1520-0450\(2002\)041<0272:AEBPRA>2.0.CO;2](https://doi.org/10.1175/1520-0450(2002)041<0272:AEBPRA>2.0.CO;2).
- Marzano, F. S., L. Roberti, S. Di Michele, A. Mugnai, and A. Tassa, 2003: Modeling of apparent radar reflectivity due to convective clouds at attenuating wavelengths. *Radio Sci.*, **38**, 1002, doi:[10.1029/2002RS002613](https://doi.org/10.1029/2002RS002613).
- Meneghini, R., and L. Liao, 2013: Modified Hitschfeld-Bordan equations for attenuation-corrected radar rain reflectivity: Application to nonuniform beamfilling at off-nadir incidence. *J. Atmos. Oceanic Technol.*, **30**, 1149–1160, doi:[10.1175/JTECH-D-12-00192.1](https://doi.org/10.1175/JTECH-D-12-00192.1).
- , H. Kim, L. Liao, J. A. Jones, and J. M. Kwiatkowski, 2015: An initial assessment of the surface reference technique applied to data from the Dual-Frequency Precipitation Radar (DPR) on the GPM satellite. *J. Atmos. Oceanic Technol.*, **32**, 2281–2296, doi:[10.1175/JTECH-D-15-0044.1](https://doi.org/10.1175/JTECH-D-15-0044.1).
- Miller, S. D., and G. L. Stephens, 1999: Multiple scattering effects in the lidar pulse stretching problem. *J. Geophys. Res.*, **104**, 22 205–22 219, doi:[10.1029/1999JD900481](https://doi.org/10.1029/1999JD900481).
- Mitrescu, C., T. L. Ecuyer, J. Haynes, S. Miller, and J. Turk, 2010: *CloudSat* precipitation profiling algorithm—Model description. *J. Appl. Meteor. Climatol.*, **49**, 991–1003, doi:[10.1175/2009JAMC2181.1](https://doi.org/10.1175/2009JAMC2181.1).
- Rodgers, C. D., 2000: *Inverse Methods for Atmospheric Sounding: Theory and Practice*. Series on Atmospheric, Oceanic and Planetary Physics, Vol. 2, World Scientific, 238 pp.
- Ryzhkov, A. V., M. R. Kumjian, S. M. Ganson, and P. Zhang, 2013: Polarimetric radar characteristics of melting hail. Part II: Practical implications. *J. Appl. Meteor. Climatol.*, **52**, 2871–2886, doi:[10.1175/JAMC-D-13-074.1](https://doi.org/10.1175/JAMC-D-13-074.1).
- Short, D. A., R. Meneghini, A. E. Emory, and M. R. Schwaller, 2015: Reduction of nonuniform beamfilling effects by multiple constraints: A simulation study. *J. Atmos. Oceanic Technol.*, **32**, 2114–2124, doi:[10.1175/JTECH-D-15-0021.1](https://doi.org/10.1175/JTECH-D-15-0021.1).
- Tanelli, S., G. F. Sacco, S. L. Durden, and Z. S. Haddad, 2012: Impact of non-uniform beam filling on spaceborne cloud and precipitation radar retrieval algorithms. *Remote Sensing of the Atmosphere, Clouds, and Precipitation IV*, T. Hayasaki, K. Nakamura, and E. Im, Eds., International Society for Optical Engineering (SPIE Proceedings, Vol. 8523), doi:[10.1117/12.977375](https://doi.org/10.1117/12.977375).
- , A. Battaglia, S. L. Durden, G. F. Sacco, O. Sy, F. Tridon, K. Mroz, and P.-E. Kirstetter, 2015: Detection and use of multiple scattering and non-uniform beam filling in DPR data. *Extended Abstracts, Precipitation Measuring Mission Science Team Meeting*, Annapolis, MD, NASA Goddard Space Flight Center. [Available upon request via e-mail from ab474@le.ac.uk.]
- Ulbrich, C. W., and D. Atlas, 1982: Hail parameter relations: A comprehensive digest. *J. Appl. Meteor.*, **21**, 22–43, doi:[10.1175/1520-0450\(1982\)021<0022:HPRACD>2.0.CO;2](https://doi.org/10.1175/1520-0450(1982)021<0022:HPRACD>2.0.CO;2).